Journal of Materials Chemistry A

ROYAL SOCIETY OF CHEMISTRY

PAPER

View Article Online
View Journal | View Issue

Check for updates

Cite this: *J. Mater. Chem. A*, 2025, **13**, 10723

Electronic structure tuning to facilitate charge transfer in Z-scheme mediated CuO/Se@WO_3 aided by synchronized $Cu(OH)_2$ for efficient overall water splitting†

Nitul Kalita, Upasana Nath, Anjana Singha, Manabendra Sarma and Mohammad Qureshi *

This work presents electronic structural tuning of metal oxides within a CuO/Se@WO_3/$Cu(OH)_2$ catalyst on Ni foam for efficient and sustainable electrocatalytic overall water splitting, addressing key limitations of scarce noble metal catalysts. A dendritic CuO layer is electrodeposited, followed by Se doping in WO_3 (Se@WO_3), forming a stable p–n junction that enhances the interfacial charge transfer for improved HER and OER activity. Selenium doping optimizes band alignment, enabling a more facile Z-scheme electron transfer pathway with CuO, minimizing electron–hole recombination. An additional $Cu(OH)_2$ layer acts as a hole extractor, further enhancing process kinetics, achieving Tafel slopes of 35 mV dec^{-1} (OER) and 45 mV dec^{-1} (HER). The modified catalyst achieved overpotentials as low as 202 mV for the OER and 55 mV for the HER at a current density of 10 mA cm^{-2}, surpassing traditional RuO_2 (for the OER) and comparable to Pt/C (for the HER) benchmarks. Density functional theory (DFT) calculations confirmed that Se doping increases the electron density at W sites and reduces the band gap, enhancing the OER through a Z-scheme aided electron–hole separation in the presence of the $Cu(OH)_2$ hole extraction layer. Gibbs free energy calculations for hydrogen adsorption indicate a ΔG_{H^*} of −0.17 eV, representing favorable HER kinetics. From the distribution of relaxation time (DRT) analysis, the time constants associated with various relaxation processes indicate a faster diffusion and charge transfer kinetics across the interfaces. These findings highlight the potential of CuO/Se@WO_3/$Cu(OH)_2$ as a low-cost, high-performance catalyst for durable hydrogen and oxygen production from water splitting.

Received 22nd January 2025
Accepted 6th March 2025

DOI: 10.1039/d5ta00627a

rsc.li/materials-a

1. Introduction

Electrocatalytic water-splitting is widely regarded as a promising method for converting renewable energy into hydrogen fuel. In this process, hydrogen and oxygen are produced using a water electrolyser, which consists of a cathode for the hydrogen evolution reaction (HER) and an anode for the oxygen evolution reaction (OER).[1] However, since the catalytic mechanisms for the HER and OER differ significantly, catalysts that are efficient for the HER typically perform poorly for the OER, and *vice versa*. Currently, the leading technology involves using platinum-based catalysts for the HER and IrO_2/RuO_2 catalysts for the OER to speed up the reactions.[2] Despite their effectiveness, the high cost of these noble metals poses a challenge for commercialization. Additionally, using distinct materials for the cathode and anode not only makes the production more complex but also raises manufacturing costs and increases the risk of cross-contamination. As a result, there is a strong focus on developing a single, versatile catalyst made from earth-abundant materials to simplify the process and reduce expenses. In recent years, significant research has focused on first-row transition metals, particularly nickel (Ni),[3] iron (Fe),[4] and cobalt (Co),[5] for their exceptional role in electrocatalytic overall water splitting, which have been predominantly studied in the form of hydroxides,[6] oxides,[7] sulfides,[8] chalcogenides,[9] and phosphides.[10] Different modification techniques, such as elemental doping, heterojunction formation, surface functionalization, and nanostructuring, have been employed to enhance their catalytic properties.[1]

From the recent studies it is well-known that incorporating electronegative chalcogens or pnictogens (X = N, P, S, Se) into transition metals can induce localized negative charges within the M–X surface structures.[11] This enhances the initial adsorption of H^+ under acidic conditions or H_2O in alkaline environments. Additionally, it modulates the electronic structure near the surface, leading to a weakened M–H bond and reduced energy barriers for the hydrogen evolution reaction (HER). The

Department of Chemistry, Indian Institute of Technology Guwahati, India. E-mail: mq@iitg.ac.in

† Electronic supplementary information (ESI) available. See DOI: https://doi.org/10.1039/d5ta00627a

oxygen evolution reaction (OER) in these materials typically takes place at high-valence metal active sites that form during anodic polarization *in operando*. Unfortunately, this anodic process often results in oxidative corrosion and structural changes in the M–X materials.[12,13] Likewise, the HER catalytic performance of M–X materials gradually deteriorates due to the compositional and structural changes caused by corrosion. This problem becomes more severe when the electrolyzer is powered by intermittent renewable sources like solar or wind energy, where frequent power interruptions and shutdowns lead to depolarization and reversed currents, accelerating electrode degradation.[2]

Thus, developing low-cost, durable catalysts with intrinsic active sites capable of efficiently catalyzing both HER and OER processes is highly challenging but essential for achieving sustained water-splitting under intermittent conditions. Despite numerous modifications made to catalytic systems to enhance the electrocatalytic performance for overall water splitting, one particular domain remains relatively underexplored, where tuning of the electronic band gap at the heterojunctions between two distinct materials has been done.[14,15] In photocatalytic processes, the modification and tuning of band gaps have been extensively studied. However, in electrocatalysis, this area remains largely underexplored, as many photocatalytic metal oxides and sulfides—such as TiO_2,[16] WO_3,[17] ZnO,[18] SnO_2,[19] CeO_2,[20] $BiVO_4$,[21] CdS,[22] ZnS,[23] MoS_2 (ref. 24) *etc.*— exhibit poor electrocatalytic activity.

There are only a handful of reports that focus on tuning band positions; for instance, Zeng *et al.*[14] enhanced NiFe–OH's OER activity by modifying band positions and forming a MnCo–CH@NiFe–OH p–n junction, which improved electron transfer and OER energetics. This resulted in up to 10-fold and 500-fold higher OER performance compared to NiFe–OH and MnCo–CH, respectively, and outperformed Pt/C||RuO_2 in overall water electrolysis. Guo *et al.*[25] developed a nitrogen-vacancy-rich Co_2N/CoP@CC p–n junction, achieving excellent HER and OER activities with overpotentials of 44 mV and 227 mV, respectively, and a water-splitting potential of 1.5 V at 10 mA cm^{-2} in alkaline medium. DFT calculations suggest that the enhanced electrocatalytic performance is due to the synergy of nitrogen vacancies and the built-in electric field from the p–n interfaces, promoting electron transfer and optimizing intermediate adsorption. A very recent study by Adhikari *et al.*[26] introduced a promising approach to boost electrocatalytic performance by constructing a p–n junction in a free-standing $MnCo_2O_{4.5}$@-Ni_3S_2 on Ni-foam, enhancing electron transfer for urea-assisted electrocatalytic water splitting (UOR). The catalyst exhibited superior OER performance with an overpotential of 240 mV, dropping to 30 mV for the UOR, due to the optimized band structure, improved electrical conductivity, and increased active sites. Additionally, *in situ* formation of NiOOH from Ni_3S_2 further boosted electrocatalytic activity through surface reconstruction.

In this study, we present a strategy for employing a photoactive material as a cocatalyst in electrocatalytic overall water splitting, achieved by precise tuning of its electronic band gap and band position *via* doping. Herein, we first electrodeposited a dendritic CuO layer onto a Ni-foam substrate, followed by the deposition of a selenium-doped WO_3 (Se@WO_3) layer, forming a p–n junction between the two layers. The idea behind creating this p–n junction is to achieve rapid charge carrier transfer at the interface, driven by the differences in work functions and Fermi energy levels (E_f).[14,27] The built-in electric field causes electrons to flow from the higher E_f (n-type semiconductor) to the lower E_f (p-type semiconductor) until thermal equilibrium is established.[28] This interfacial charge redistribution enhances the adsorption and desorption of hydrogen and oxygen intermediates in an alkaline electrolyte, thereby significantly boosting HER and OER activities. Apart from creating the p–n junction, a significant modification in this study is the Se doping of WO_3, where approximately 6% of the oxygen atoms in the crystal structure are replaced by selenium. This substitution enhances the water-splitting performance by introducing metallic character into WO_3, leading to a band gap reduction of about 0.54 eV. The narrower band gap shifts the conduction band of WO_3 closer to the valence band of CuO, facilitating a Z-scheme electron transfer mechanism. This mechanism promotes efficient electron transfer from the n-type Se@WO_3 to the p-type CuO, thereby reducing the likelihood of electron–hole recombination. To address the relatively high charge transfer resistance between the Se@WO_3 surface and the electrolyte, an additional $Cu(OH)_2$ layer was electrodeposited. This layer exhibits a needle-like morphology emerging from the p–n junction, as confirmed by FESEM imaging. This $Cu(OH)_2$ layer functions as a hole extractor from the p–n junction, effectively reducing the charge transfer resistance at the electrode–electrolyte interface. These improvements have been validated through both theoretical and experimental analyses. The rationale behind adding $Cu(OH)_2$ as the charge extractor to improve the kinetics of the electrolysis process lies in the synchronization of the redox couple (Cu/Cu^{2+}) that is occurring in between the CuO and $Cu(OH)_2$ layers. It has already been reported that if there is an identical metal atom present in two layers (CuO and $Cu(OH)_2$ in the present scenario), the layers become redox active under the same potential which helps in reducing the overpotential value.[29]

In this study, we achieved significant reductions in overpotential for both the oxygen evolution reaction (OER) and hydrogen evolution reaction (HER) using a CuO/Se@WO_3/$Cu(OH)_2$ catalyst on Ni foam. The overpotential values reached as low as 202 mV for the OER and 55 mV for the HER at a current density of 10 mA cm^{-2}. Kinetic analysis *via* Tafel slope measurements demonstrated values of 35 mV dec^{-1} for the OER and 45 mV dec^{-1} for the HER, indicating favorable reaction kinetics. Compared to benchmark catalysts, the synthesized catalyst outperformed RuO for the OER and showed nearly equivalent performance to Pt/C for the HER, highlighting its superior electrocatalytic efficiency. The catalyst's mechanism and performance parameters were further supported by density functional theory (DFT) calculations. The electronic band structure and partial density of state (PDOS) plots of WO_3 and Se@WO_3 highlight the lowering of the band gap after Se-doping, thereby enhancing its electronic conductivity. The valence band state of Se@WO_3 approaches the E_f, mostly due to

the W_d (d-orbitals of W) favoring electron transfer. Moreover, the electron density of the W atom increases upon Se doping. The increase in charge density at W_d and the reduction in band gap promote the energetically favorable d–d electron transfer from the W_d orbitals of WO_3 to the Cu_d orbitals of CuO, enhancing the Z-scheme electron transfer efficiency. Furthermore, the ΔG_{H^*} of CuO/Se@WO_3/$Cu(OH)_2$ is −0.17 eV ($|\Delta G_{H^*}| <$ 0.20 eV), indicating better HER catalytic activity as compared to CuO/WO_3/$Cu(OH)_2$ with ΔG_{H^*} of 0.21 eV, consistent with the experimental results.[30] Additionally, the overpotential for the OER is also reduced due to the multifunctional active sites formed at the interface, particularly attributed to the hole-extracting properties of $Cu(OH)_2$ from the p–n junction. Thus, through the combination of different physical and electrochemical characterization methods, this study demonstrates the remarkable physical and electrochemical performance and stability of CuO/Se@WO_3/$Cu(OH)_2$ for both HER and OER processes.

2. Experimental section

2.1 Materials

For the synthesis of the heterogeneous catalyst, the Ni-foam substrate was purchased from Hi-TECH Scientific Equipment India. For the synthesis of CuO, copper(II) sulphate was purchased from Sigma-Aldrich. Hydrochloric acid (36%) and sulfuric acid (98%) were bought from Finar, India. For the synthesis of WO_3, H_2WO_4 (99%), oxalic acid ($H_2C_2O_4$) and urea (H_2NCONH_2) were purchased from Sigma-Aldrich, whereas acetonitrile solvent was bought from Finar, India. For the synthesis of $Cu(OH)_2$, Cu-foil was procured from Sigma-Aldrich. Potassium hydroxide (KOH) used in the electroanalysis was purchased from Merck.

2.2 Material synthesis

Dendritic copper hydroxide oxide was grown on the nickel foam substrate through an electrodeposition method. The stock solution was prepared by dissolving 0.05 M $CuSO_4 \cdot 5H_2O$, 1 M H_2SO_4, and 2 M HCl in 50 mL of deionized water, followed by vigorous stirring at ambient temperature for 15 minutes to ensure complete mixing. The electrodeposition was carried out in a two-electrode setup, where cleaned Ni foam (1 cm^2) was used as the anode and a platinum (Pt) electrode served as the cathode. A direct current (DC) power supply was employed to apply a current density of 1 A cm^{-2} for 10 seconds. Post-deposition, the film was thoroughly rinsed with deionized water and ethanol to remove any residual contaminants, and subsequently dried under vacuum at room temperature.

In the subsequent step for synthesizing selenium-doped WO_3, a layer of tungsten hydroxide was deposited onto the prefabricated dendritic copper hydroxide using a hydrothermal process. A precursor solution was prepared by mixing 3 mL of H_2WO_4 (0.05 M) and 0.02 g of urea in 12.5 mL of acetonitrile, followed by stirring for 30 minutes to ensure complete dissolution. Subsequently, 0.5 mL of concentrated HCl (6 M) was added to the mixture, and the solution was stirred for an additional 15 minutes. The resulting solution was then transferred into a 25 mL stainless steel autoclave, where the dendritic copper hydroxide deposited on Ni-foam was immersed. The hydrothermal treatment was carried out at 180 °C for 2 hours. After the reaction, the obtained films were thoroughly rinsed with deionized water and ethanol to remove any residual impurities.

Prior to converting the hydroxide to the oxide form *via* calcination, selenium doping was performed using an electrochemical approach. A solution was prepared by dissolving 1 mM SeO_2 and 100 mM NaCl as the supporting electrolyte in 100 mL of deionized water, followed by stirring at 60 °C for 30 minutes to ensure complete dissolution. This solution served as the electrolyte for the electrochemical doping. The working electrode consists of the above prepared material, with platinum and Ag/AgCl functioning as the counter and reference electrodes, respectively. Selenium deposition was carried out using cyclic voltammetry for 10 cycles from 0 to −0.8 V at a sweep rate of 10 mV s^{-1}. The degree of doping achieved varied based on the number of cycles performed (see ESI Fig. S7†). The next step involved calcining the synthesized electrode at 400 °C with a ramp rate of 2 °C min^{-1} for two hours, converting the metal hydroxides to their respective oxides, thereby forming the CuO/Se@WO_3 composite on the Ni foam substrate. In the final step, a needle-like $Cu(OH)_2$ hole-extracting layer was deposited onto the CuO/Se@WO_3 structure using an anodization method. A three-electrode system was employed, consisting of as-synthesized CuO/Se@WO_3 as the working electrode, Cu-foil as the counter electrode, and an Hg/HgO reference electrode, all immersed in a 1 M KOH solution. Electrodeposition was carried out by applying a constant potential of −0.1 V for 100 seconds, achieving the desired morphology, as confirmed by FESEM imaging. The resulting CuO/Se@WO_3/$Cu(OH)_2$ electrode was thoroughly rinsed with deionized water and ethanol, then stored under vacuum for subsequent electroanalysis.

2.3 Material characterization

The X-ray diffraction (XRD) analysis was performed using a Rigaku SmartLab diffractometer equipped with a copper K_α radiation source ($\lambda = 1.54$ Å) using a 9 kW rotating anode. XRD patterns were collected over a 2θ range of 5–80° with a fixed scan rate of 5° s^{-1}. Morphological characterization of the samples was conducted *via* field emission scanning electron microscopy (FESEM) using a Zeiss Gemini or Sigma model, operated at 5 kV. Additionally, field emission transmission electron microscopy (FETEM) analysis was carried out with a JEOL JEM-2100F transmission electron microscope at 200 kV. To determine the faradaic yield and quantify the evolved gases, gas chromatography (GC) was employed using an Agilent 7820A instrument.

2.4 Electrochemical measurements

All the electrochemical measurements were performed using an Interface 1010E potentiostat in a three-electrode setup with 1 M KOH (pH 13.1) as the electrolyte, fabricated electrode as the working electrode, graphite as the counter electrode, and Hg/HgO as the reference. LSV was conducted from 0.2 to 1.2 V

versus Hg/HgO at 5 mV s^{-1}, while EIS measurements spanned 0.1 to 10^5 Hz at fixed potentials. CV for the determination of electrochemical active surface area was carried out between 1.15 and 1.22 V *vs.* RHE with scan rates of 1–6 mV s^{-1}. All potentials were converted to the RHE scale.

$$E_{RHE} = E_{Hg/HgO} + 0.059 \times pH + E^0_{Hg/HgO}$$

Here, E_{RHE} represents the RHE potential, while $E^0_{Hg/HgO}$ is 0.098 V at 25 °C. $E_{Hg/HgO}$ denotes the potential measured relative to the Hg/HgO reference electrode, and pH refers to the pH of the electrolyte used.[31]

2.5 Computational methodology

Density functional theory (DFT) calculations were carried out using generalized gradient approximation with Perdew–Burke–Ernzerhof (PBE) functional *via* Vienna *ab initio* simulation package (VASP).[32–34] The projector-augmented wave describes the interaction behavior of the ion and electron.[35] A plane wave basis was obtained for all calculations through a kinetic energy cutoff of 600 eV and a Monkhorst–Pack grid of 2 × 2 × 1.[36] To reduce the lattice mismatch 2 × 2, 2 × 2 and 3 × 1 supercells of CuO, WO_3, and $Cu(OH)_2$ are used with the cell dimension of a = 10.61 Å and b = 10.41 Å. The detailed description (cell dimension and the interlayer distances) of the construction of the heterostructure is presented in Section 1 of the ESI.† A 40 Å vacuum was added along the *c*-axis to prevent image interactions generated by periodic boundary conditions. Grimme's proposed empirical vdW correction approach (DFT-D3) was applied to explain the interlayer long-range interactions.[37] The final structures of CuO/WO_3/$Cu(OH)_2$ and CuO/Se@WO_3/$Cu(OH)_2$ are shown in Fig. S4 (ESI).† Gibbs free energy (ΔG) was calculated to understand the HER and OER activity of the systems according to eqn (1).[38]

$$\Delta G = \Delta E + \Delta ZPE - T\Delta S \quad (1)$$

Here, ΔE, ΔZPE, and $T\Delta S$ represent the adsorption energy of all the reaction intermediates, zero-point energy, and entropy change of the intermediates at 298.15 K, respectively, resulting from DFT calculations. Nørskov *et al.* developed the computational hydrogen electrode (CHE) model to measure the free energy (ΔG) of the formation of all intermediates in electrocatalytic processes.[39]

For the HER,[40]

$$* + H_2O + e^- = H* + OH^-$$

For the OER,[41,42]

$$\Delta G_1 = * + OH^- = HO* + e^-$$

$$\Delta G_2 = HO* + OH^- = O* + H_2O + e^-$$

$$\Delta G_3 = O* + OH^- = HOO* + e^-$$

$$\Delta G_4 = HOO* + OH^- = * + O_2 + H_2O + e^-$$

The overpotential (η) of the OER can be evaluated using the following formula:

$$\eta = \frac{\max\{\Delta G_1, \Delta G_2, \Delta G_3, \Delta G_4\}}{e} - 1.23\ V$$

3. Results and discussion

In this work the electrochemical activity and performance were enhanced by increasing the electrochemically active surface area through morphological tuning and creating a heterojunction that supports Z-scheme charge separation for efficient HER and OER. FESEM analysis presents the morphological characteristics of the synthesized materials. Fig. 1(a)–(c) illustrate the structural features of CuO, WO_3, and $Cu(OH)_2$, respectively. The FESEM images reveal that the dendritic structure of CuO, serving as the base layer, provides an extensive electrocatalytic active surface area of 0.52 cm^2 mg^{-1} that has been derived from ECSA calculation (ESI† eqn (2)). Fig. 1(d) and (e) show WO_3 and Se-doped WO_3 deposited on CuO, where a nano-block morphology is observed on the CuO surface, indicating that Se doping does not significantly alter the morphology. Fig. 1(f) presents the final heterostructure, showing the needle-like morphology of $Cu(OH)_2$, grown *via* anodization, extending from the p–n heterojunction. The morphological characteristics were further verified using FETEM, as shown in Fig. 1(g). Fig. 1(h) and (i) represent the high resolution TEM images obtained from the dendritic CuO and WO_3/$Cu(OH)_2$ structures, with *d*-spacing values determined through inverse fast Fourier transform (IFFT) corresponding to specific crystal planes. Elemental mapping of the CuO/Se@WO_3/$Cu(OH)_2$ composite was performed using FESEM-EDX (Fig. 1(k)–(n)), confirming the uniform distribution of all constituent elements. Additionally, scanning transmission electron microscopy energy-dispersive spectrometry (STEM-EDS) (ESI, Fig. S8†) analysis of Se-doped WO_3 (Se@WO_3) was conducted to determine the Se doping level relative to the total oxygen content in the WO_3 lattice. The highest performance for the HER and OER was observed when approximately 6% of the total oxygen in the lattice was substituted with selenium, corresponding to a total substitution of about 4.7% relative to the complete WO_3 lattice. This doping percentage was used in subsequent theoretical calculations to gain a deeper understanding of the composite material's properties. To obtain more accurate measurements, we have performed ICP-MS (Inductively Coupled Plasma Mass Spectrometry) analysis for Se-doped WO_3 to quantify the atomic concentration of Se doping. The ICP-MS measurements were conducted on Se doped WO_3, and the W and Se concentration was found to be 756.5 ppb and 58 ppb respectively. Thus, the final composition of Se-doped WO_3 is determined to be $WO_{2.82}Se_{0.18}$. From the calculation of defect formation energy, a value as low as 1.69 eV per atom was obtained (see ESI Section 1.3†), indicating a thermodynamically favorable doping process.

The synthesized compounds' phase formation was confirmed using powder X-ray diffraction (Fig. 1(j)). The XRD analysis verified the pure formation of CuO on the Ni foam

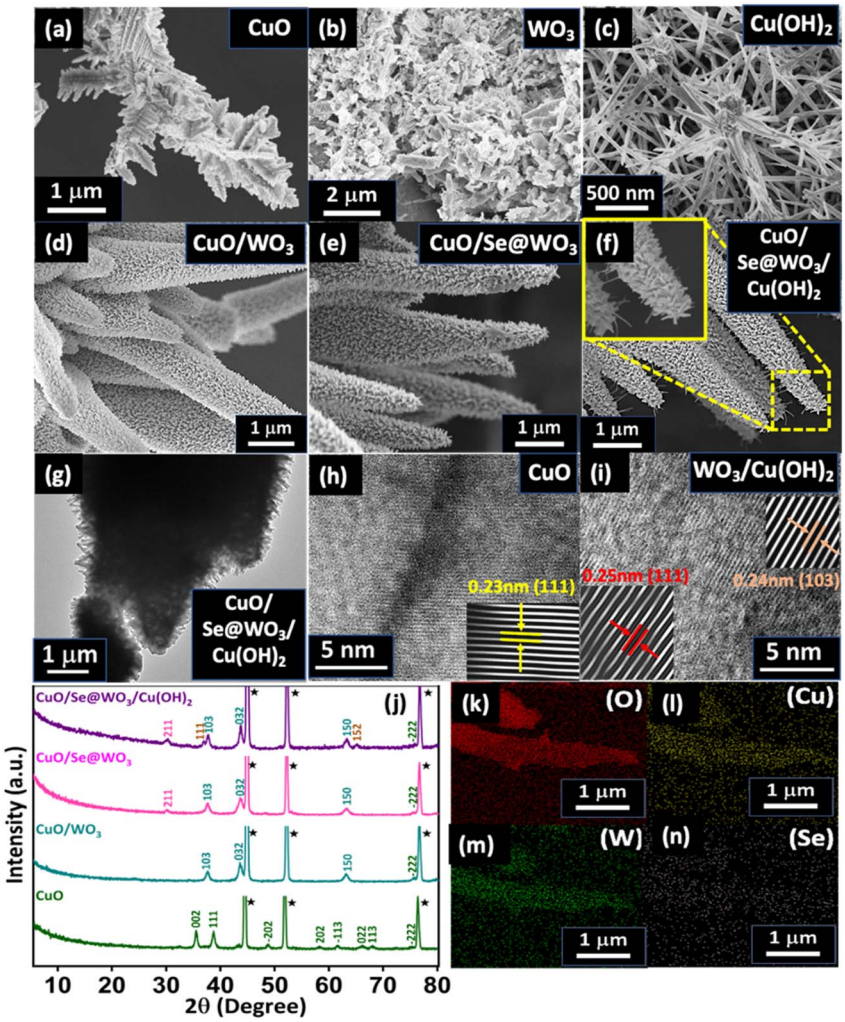

Fig. 1 (a–c) FESEM image of dendritic CuO, WO_3 nano blocks and $Cu(OH)_2$ needle individually deposited over Ni-foam; (d and e) FESEM image of CuO/WO_3 with and without Se doping onto WO_3; (f) FESEM image of the CuO/Se@WO_3/$Cu(OH)_2$ composite; (g) FETEM image of CuO/Se@WO_3/$Cu(OH)_2$; (h) HRTEM image of CuO representing the (111) crystal plane; (i) HRTEM image of WO_3/$Cu(OH)_2$ showcasing the (103) crystal plane from WO_3 and (111) from $Cu(OH)_2$ with the inset displaying the corresponding IFFT pattern; (j) XRD plot representing CuO (green), CuO/WO_3 (cyan), Se@WO_3 (pink) and CuO/Se@WO_3/$Cu(OH)_2$ (violet). (k–n) FESEM-EDX mapping showing the homogeneous distribution of O, Cu, W and Se.

substrate, as indicated by its characteristic peaks at 2θ values 35.5°, 38.7°, 48.8°, 58.2°, 61.8°, 66.1°, 67.9°, and 75.2° corresponding to the (002), (111), (−202), (202), (−113), (022), (113), and (−222) planes of CuO (ICSD No. 00-002-1040).

Following the deposition of the next layer, XRD measurements were conducted for both CuO/WO_3 and CuO/Se@WO_3 composites. The XRD pattern for CuO/WO_3 exhibited peaks at 2θ values 37.2°, 43.3°, and 62.8°, corresponding to the (103), (032), and (150) planes of the monoclinic phase of WO_3 (ICSD No. 00-043-1035) and another peak was observed at 75.2°, corresponding to the (−222) plane from CuO. For a comprehensive comparative study, we have also analyzed and compared the XRD data of pure WO_3 with Se-doped WO_3 (see ESI S5†). For the Se@WO_3, peaks were observed at 2θ values 29.7°, 37.2°, 43.3°, and 62.8°, which corresponded to the (211), (103), (032), and (150) planes of WO_3, in agreement with ICSD No. 01-072-0677. The cell volume associated with WO_3 according to the ICSD card no. 00-043-1035 is 422.88 Å^3, while the cell volume reported in the ICSD card 01-072-0677 is slightly larger at 423.68 Å^3. This increase is attributed to the substitution of approximately 6% of oxygen atoms with selenium, which has a larger atomic radius than oxygen. To further investigate this cell volume expansion, Rietveld refinement of the XRD data was performed (see ESI Section 7†), excluding peaks originating from the Ni foam substrate. The refined cell volumes closely matched the reported values, with 422.79 Å^3 for WO_3 and 423.82 Å^3 for Se@WO_3, supporting the observed increase due to selenium incorporation.

Electrochemical measurements reveal that the formation of a p–n heterojunction between p-type CuO and n-type Se@WO_3, along with a $Cu(OH)_2$ hole-extracting layer, significantly improves overall water splitting performance. The semiconductor nature was confirmed through Mott–Schottky analysis (Fig. S10†), the negative slope of CuO identified it as p-type

and the positive slope of WO_3 and Se@WO_3 indicates that it is an n-type semiconductor. Linear sweep voltammetry (LSV) data (Fig. 2(a and d)) indicate that the CuO/Se@WO_3/Cu$(OH)_2$ composite exhibits an overpotential of 202 mV for the oxygen evolution reaction (OER) and 55 mV for the hydrogen evolution reaction (HER). The OER performance surpasses that of the benchmark catalyst RuO_2, while the HER activity approaches the benchmark value achieved by Pt/C. The bar diagram in Fig. 2(b and e) illustrates the overpotential values for the oxygen evolution reaction (OER) and hydrogen evolution reaction (HER). After doping selenium (Se) into n-type WO_3, a reduction in overpotential was observed, with a reduction of 28 mV for the OER and 55 mV for the HER with respect to the undoped counterpart, *i.e.*, CuO/WO_3/Cu$(OH)_2$. This improvement can be attributed to two main factors: first Se doping imparts a metallic character to WO_3 by increasing the density of states at the E_f, as revealed by theoretical projected density of states (PDOS) analysis. Experimental results also confirm a significant band gap reduction, aligning with theoretical predictions. Second, the reduced band gap facilitates a Z-scheme mechanism, enabling effective separation of electron–hole pairs, thereby enhancing the efficiency of the HER and OER within their respective potential ranges. When comparing the electrochemical performance of the composite without the Cu$(OH)_2$ hole-extracting layer, higher overpotential values were observed for both the OER (Fig. 2(b)) and HER (Fig. 2(e)). This can be attributed to the intrinsic properties of the Cu$(OH)_2$ layer, where it continuously extracts holes generated at the p–n junction and transfers them

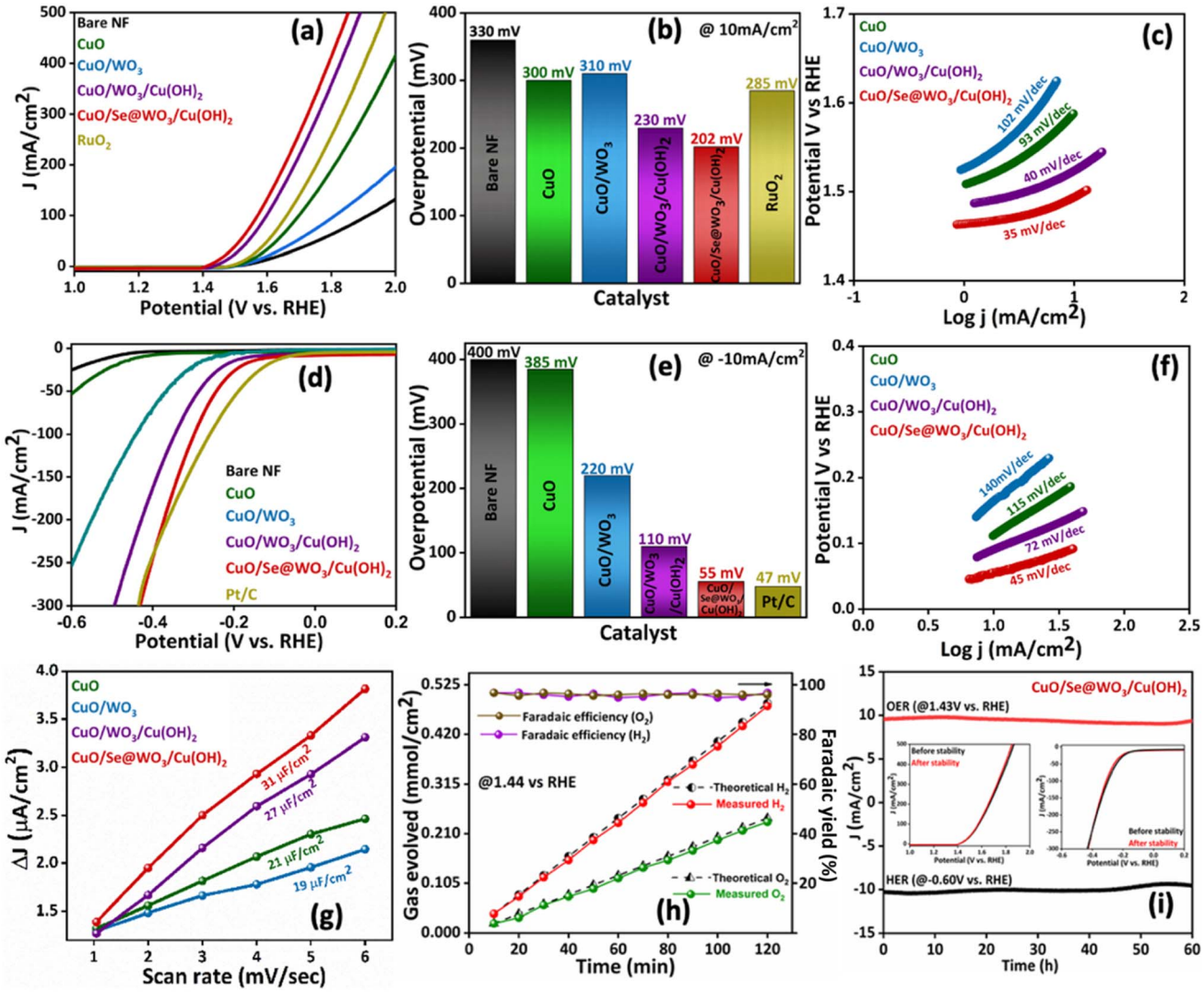

Fig. 2 (a and d) LSV polarisation curves for the OER and HER representing bare Ni-foam, CuO, CuO/WO_3, CuO/WO_3/Cu$(OH)_2$ and CuO/Se@WO_3/Cu$(OH)_2$ compared with the benchmark catalyst RuO for the OER and Pt/C for the HER; (b and e) bar diagram for the OER and HER representing overpotentials @10 mA cm^{-2} derived from figure (a) and (d); (c and f) corresponding Tafel slope of CuO, Cu/WO_3, CuO/WO_3/Cu$(OH)_2$ and CuO/Se@WO_3/Cu$(OH)_2$ derived from the LSV curve taken at a sweep rate of 5 mV s^{-1} in 1 M KOH; (g) C_{dl} plot of CuO, Cu/WO_3, CuO/WO_3/Cu$(OH)_2$ and CuO/Se@WO_3/Cu$(OH)_2$; (h) faradaic yield plot for CuO/Se@WO_3/Cu$(OH)_2$ for O_2 and H_2 at 1 M KOH, (i) stability curve showing the stability of CuO/Se@WO_3/Cu$(OH)_2$ at 1 M KOH at an applied potential of 1.43 V *vs.* RHE for the OER and −0.60 V *vs.* RHE for the HER for 60 hours.

into the electrolyte, facilitating a faster water oxidation process. Consequently, the counter electrons generated are directed through the external circuit to the cathode, where they contribute to the water reduction process. The significance of a third metal hydroxide layer in the OER is evident from the overpotential values in Fig. 2(b). Although CuO/WO_3 has a p–n heterojunction that could enhance charge separation and accumulation, CuO alone shows a slightly lower overpotential (300 mV) compared to CuO/WO_3 (310 mV). This suggests that an electroactive layer above the p–n junction is necessary to effectively extract charges generated at the heterojunction.

The water oxidation kinetics of the electrocatalyst were assessed through Tafel slope analysis, which provides insights into the charge transfer efficiency (see ESI Section 9†). As shown in Fig. 2(c and f), the addition of a $Cu(OH)_2$ layer significantly decreases the Tafel slope for the OER from 102 mV dec^{-1} (CuO/WO_3) to 40 mV dec^{-1} ($CuO/WO_3/Cu(OH)_2$), indicating enhanced charge transfer kinetics due to the metal hydroxide layer acting as a hole extractor. A similar improvement was observed in the HER, with the Tafel slope dropping from 140 mV dec^{-1} to 72 mV dec^{-1}, confirming an increased charge transfer rate with the $Cu(OH)_2$ addition. The Tafel slope decreases further from 40 mV dec^{-1} to 35 mV dec^{-1} for the OER and from 72 mV dec^{-1} to 45 mV dec^{-1} for the HER between $CuO/WO_3/Cu(OH)_2$ and $CuO/Se@WO_3/Cu(OH)_2$, highlighting the role of Se doping in enhancing water electrolysis performance by improving the charge separation process.

The improvement in electrochemical performance is often due to increase in electroactive sites within the compounds. To quantify the electrochemically active surface area (ECSA) of each electrocatalyst, double-layer capacitance (C_{dl}) values were measured through cyclic voltammograms (CVs) in the non-faradaic region at varying scan rates (see ESI Fig. S6†). Performing CVs at low scan rates allows for optimal adsorption of charged species on the electrode surface, providing deeper insight into double-layer formation. As shown in Fig. 2(g), C_{dl} increases significantly from 19 μF cm^{-2} for CuO/WO_3 to 27 μF cm^{-2} for $CuO/WO_3/Cu(OH)_2$, attributed to the additional electroactive and morphologically beneficial $Cu(OH)_2$ layer and trending with the values associated with the overpotentials. Following Se doping, $CuO/Se@WO_3/Cu(OH)_2$ exhibits an even higher C_{dl} of 31 μF cm^{-2} implying the increase in electroactive sites on WO_3 due to the doping process, which imparts additional metallic character to WO_3.

Enhancement in electrochemical performance is often linked to efficient charge transfer kinetics at the electrolyte–electrode interface. Electrochemical impedance spectroscopy (EIS) was used to assess charge mobility at the electrode–electrolyte interface by measuring charge transfer resistance (R_{ct}). As shown in Fig. S12 (ESI),† EIS conducted at 1.43 V *vs.* RHE provides Nyquist plots for the individual catalysts, and the resulting R_{ct} values align with the Tafel slope trends, illustrating improvements in reaction kinetics. According to eqn (S5) (ESI),† the Tafel slope is inversely proportional to the material's charge transfer coefficient (*i.e.*, Tafel slope $\propto 1/\alpha$). The Nyquist plot reveals that the $CuO/Se@WO_3/Cu(OH)_2$ composite exhibits the lowest R_{ct} value, at 4.2 Ω, this superior charge transfer in p–n heterojunction electrocatalysts is driven by the built-in electric field enhancing charge separation and transport, while the metal hydroxide top layer ensures a high charge transfer coefficient. $CuO/WO_3/Cu(OH)_2$ shows a slightly higher R_{ct} value of 5.3 Ω, due to less effective charge separation *via* the Z-scheme mechanism. In comparison, CuO/WO_3 without the $Cu(OH)_2$ hole extracting layer has a higher R_{ct} value of 7.1 Ω, indicating reduced charge transfer efficiency at the electrolyte interface.

A good electrocatalyst should have high stability to be used under harsh conditions. To test the durability of the synthesized electrocatalyst, chronoamperometry measurements were performed at a fixed potential of 1.43 V *vs.* the RHE for the OER and −0.60 V *vs.* RHE for the HER. Fig. 2(i) shows the stability of $CuO/Se@WO_3/Cu(OH)_2$ with negligible decrease in the current density even after 60 h of continuous operation. The inset shows the constancy in the LSV curve of the composite material toward the OER and HER measured before and after the stability test. To further test the durability of the catalyst, the composite material was tested for 1000 cycles of cyclic voltammetry measurement in the faradaic regions (see ESI Fig. S13†). After the analysis it can be confirmed that the electrocatalyst is highly stable as there is negligible change in the current density values.

To understand the time constants associated with different relaxation processes across the interfaces, we have analyzed the distribution of relaxation time (DRT) constants using the DRT tool in MATLAB based on the data of AC impedance spectra (Fig. S12†).[43,44] This analysis enables the identification of distinct kinetic processes, each exhibiting characteristic relaxation behaviors that are observable across multiple timescales. Analyzing timescale information in water splitting offers insights into key kinetic challenges, including ionic conduction, charge transfer, diffusion control, interfacial evolution, and other previously unexplored kinetic processes. The Distribution of Relaxation Times (DRT) method enables direct identification of the time constants associated with major electrochemical processes, simplifying impedance analysis and greatly enhancing the accuracy of kinetics interpretation within these timescales. The detailed methodology involved in DRT analysis has been provided in Section 14 of the ESI.† The relationship between the distribution function and impedance is defined by eqn (2).

$$Z(\omega) = R_{\infty} + R_{pol}\int_{-\infty}^{\infty} \frac{\Gamma(\log(\tau))}{1 + i\omega\tau} d(\log(\tau)) \quad (2)$$

In this context, $Z(\omega)$ represents the total impedance, R_{∞} is the series resistance, R_{pol} denotes the total polarization resistance of the processes, Γ is the distribution function of relaxation times, τ is the relaxation time, and ω is the frequency of the applied input.

Following the application of DRT analysis to the EIS data, the resulting DRT plot (Fig. 3(e)) reveals three distinct peaks, each corresponding to the resistance contribution of an individual electrochemical process to the electrode's total polarization resistance. The time constant (τ) is unique to each polarization process, with the area under each peak indicating the extent of polarization resistance (R_P) contribution of a specific electrochemical process to the overall cell polarization. Thus, changes

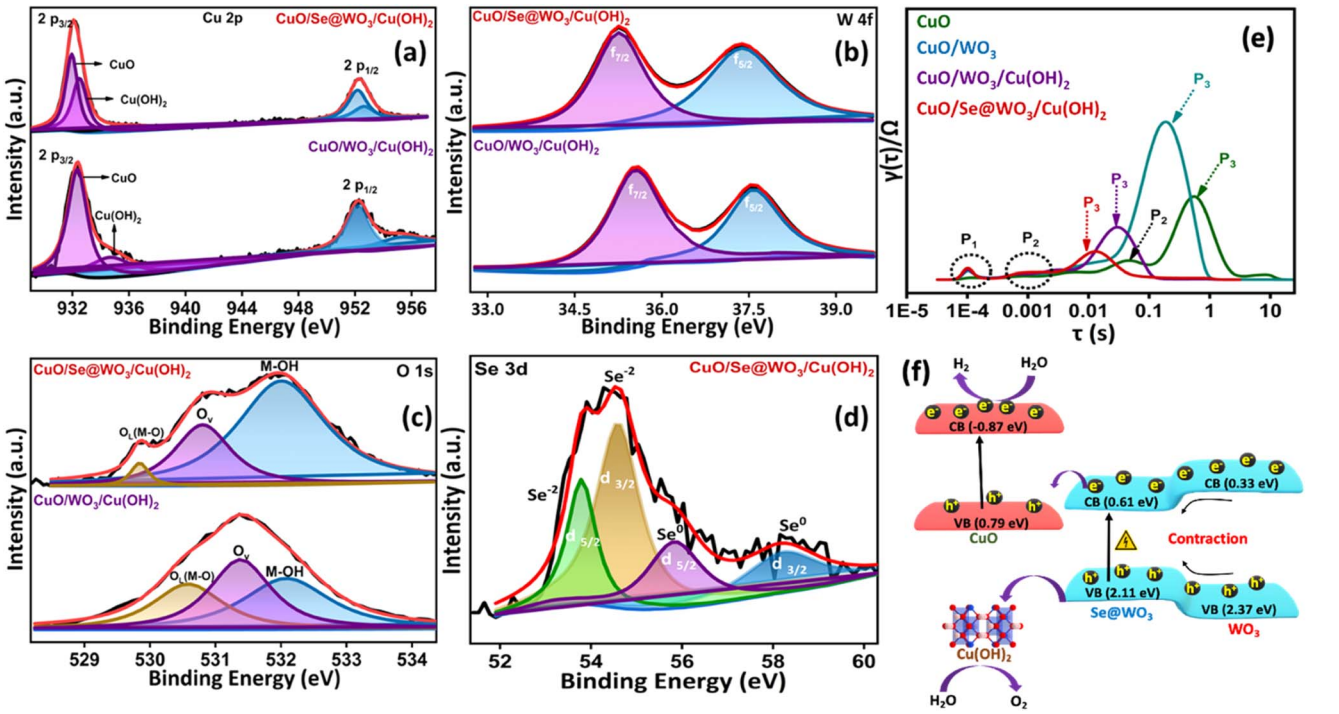

Fig. 3 High-resolution XPS spectra of (a) Cu 2p, (b) W 4f and (c) O 1s for $CuO/WO_3/Cu(OH)_2$ (bottom) and $CuO/Se@WO_3/Cu(OH)_2$ (top); (d) XPS core level spectra for Se 3d for $CuO/Se@WO_3/Cu(OH)_2$; (e) DRT analysis performed from EIS data; (f) schematic representing the electron transfer process across the heterojunction for overall water splitting.

in the DRT profile can directly reflect alterations in the nature and magnitude of the electrode reactions. Three peaks represented as P1, P2, and P3 are observed in the DRT plot, each corresponding to characteristic time constants. where P_1 represents the high-frequency semicircle, attributed to series resistance across the electrolyte and electrode interface, P_2 corresponds to the mid-frequency semicircle, associated with charge transfer reactions at the interface and P_3, in the low-frequency region, is linked to diffusion processes. Our comparative study reveals that the peaks P_3 and P_2, associated with the diffusion and charge transfer processes both have shifted to higher frequencies with reduced peak intensities in the final modified catalyst, *i.e.*, $CuO/Se@WO_3/Cu(OH)_2$. These findings indicate that ion diffusion and charge transfer kinetics are highest when the $CuO/Se@WO_3/Cu(OH)_2$ electrode is used as the electrocatalyst. This improvement is further reflected in the calculated effective resistance values as shown in Table 1. It is observed that resistance values are significantly reduced for the diffusion resistance P_3 (4.2 Ω) and charge transfer resistance P_2 (0.01 Ω) along with faster relaxation times for charge transfer processes (P_2, P_3) observed in the $CuO/Se@WO_3/Cu(OH)_2$ composite, compared to other electrode modifications highlighting its enhanced electrochemical kinetics.

Table 1 Effective resistance values calculated for various electrochemical processes across different catalytic systems

System	P_1 (Ω)	P_2 (Ω)	P_3 (Ω)
CuO@NF	1.5×10^{-5}	0.076	5.47
CuO/WO_3@NF	1.4×10^{-4}	0.014	10.55
$CuO/WO_3/Cu(OH)_2$@NF	1.2×10^{-5}	0.023	5.33
$CuO/Se@WO_3/Cu(OH)_2$@NF	**1.1×10^{-5}**	**0.01**	**4.2**

X-ray photoelectron spectroscopy (XPS) was conducted to analyse the changes in the electronic structure of $CuO/WO_3/Cu(OH)_2$ before and after Se doping. As shown in Fig. 3(a) and (b), both the Cu 2p and W 4f core-level spectra exhibit shift towards the lower binding energies after Se doping. In particular, in the Cu 2p spectrum (Fig. 3(a)), a significant shift of approximately 1.2 eV is observed for both the $2p_{3/2}$ and $2p_{1/2}$ peaks in the $Cu(OH)_2$ layer. For W 4f, a similar shift is evident, where both the peaks $4f_{5/2}$ and $4f_{7/2}$ have moved around 0.3 eV towards lower binding energy. The observed shift to lower binding energies supports the successful incorporation of Se into the WO_3 layer. Due to its lower electronegativity and greater metallic character compared to oxygen, Se can donate local electron density to neighbouring metal atoms, increasing the electron density around these atoms. This increased electron density reduces the energy required to remove electrons from the core levels, resulting in the observed shifts toward lower binding energies. Fig. 3(c) shows the O 1s core-level spectra, which display three distinct peaks from lower to higher binding energies. These peaks correspond to lattice oxygen (O_L), oxygen vacancies (O_v), and the metal hydroxides or adsorbed water molecules, respectively. Following Se doping, a prominent shift towards the lower binding energy is observed in the lattice oxygen peak. This shift is likely to occur due to oxygen atoms bonding to the metal that are replaced by less electronegative Se

atoms, which partially donate electron density to the adjacent metal and oxygen atoms, resulting in a lower binding energy for the lattice oxygen. Fig. 3(d) shows the Se 3d core-level spectra, where peaks corresponding to both Se^0 and Se^{-2} states are observed. The intensity ratio of Se^0 to Se^{-2} indicates a higher proportion of Se in the −2-oxidation state. This predominance of Se^{-2} suggests successful incorporation of Se into the crystal lattice by the substitution of O^{-2}, while the Se^0 represents undoped elemental Se.

To gain a deeper understanding of the electrocatalytic mechanism, we have conducted both experimental and theoretical analyses of the materials. Experimentally, Mott–Schottky analysis was performed on both CuO and WO_3 to identify the p–n junction. Additionally, to examine how Se doping affects the flat band potential of WO_3, we have performed Mott–Schottky analysis for Se@WO_3 as well. Further we have analyzed the Mott–Schottky plot for Se@WO_3 before and after the heterojunction formation and calculated the carrier density (N_D) (detailed calculations explained in ESI Section 8†). The calculated carrier density provides further insights into our proposed mechanism for charge separation and transfer processes. As shown in Fig. S10(a),† CuO exhibits a negative slope, confirming its p-type semiconductor nature, while WO_3 shows a positive slope (Fig. S10(b)†), characteristic of an n-type semiconductor. The Mott–Schottky analysis of Se@WO_3 also reveals a shift in flat band potential towards a higher value compared to undoped WO_3, indicating that Se doping alters the band positions for WO_3. The exact band positions and band gaps of the individual materials were determined using a combination of XPS valence band spectra (see ESI S14†) and Tauc plots (see ESI S15†) derived from ultraviolet-visible diffuse reflectance spectroscopy (UV-Vis DRS) data. For our study all the UV-Vis DRS measurements were performed over the 200–800 nm range. The band gap values were obtained by extrapolating the linear portion of each Tauc plot to the *x*-axis, where the intercept on the $h\nu$ axis gives E_g. Results indicate a band gap of 1.66 eV for p-type CuO, 2.04 eV for n-type WO_3, and a reduced band gap of 1.50 eV for Se-doped WO_3. This reduction in WO_3's band gap after Se doping has been previously discussed. After determining the band gap, our next objective was to identify the precise band positions of the materials to better understand the underlying mechanism. Although Mott–Schottky measurements can estimate band positions, they often lack accuracy due to assumptions about carrier density and ideal semiconductor behavior, which may not apply to real materials. Surface states and experimental conditions can also affect the flat-band potential, leading to inconsistencies. Therefore, XPS valence band spectra offer a more reliable method for determining valence band positions. From the XPS valence band spectra, the valence band maximum (VBM) of CuO and WO_3 were found to be 0.793 eV and 2.369 eV, respectively, determined by extrapolating the leading edge of the valence band spectrum to the baseline, representing the highest occupied energy state below the Fermi level. After Se doping, the VBM of WO_3 shifted to 2.114 eV (Fig. S14(c)†), indicating a band gap change due to the doping process. Combining the VBM data with band gap information from the above experimental approaches provides a clearer understanding of the band positions of each material in the heterojunction and their roles in the charge transfer mechanism during water splitting. For better understanding and visualization, we have added a table (see ESI Table S2†) representing the summary of the band positions of the materials determined from the Tauc plot and XPS valence band spectra.

The plausible mechanism proposed is further supported by theoretical studies, where Fig. 4(a–c) show the electronic band structure and projected partial density of states (PDOS) plots of WO_3 and Se@WO_3. The electronic band structure analysis revealed that WO_3 exhibits semiconductor properties having a band gap of 1.99 eV.[45] Additionally, it has been shown that incorporating Se atoms significantly decreases the band gap of the system to 1.42 eV. As shown in the PDOS of bulk WO_3 in Fig. 4(c), the valence and conduction bands mainly consist of O 2p and W 4d states. However, the PDOS plot of Se@WO_3 shows that the p-orbital of the Se-atom overlaps with the W_p and W_d orbitals at the valence band region closer to the E_f. Additionally, the valence band state of Se@WO_3 approaches the E_f mainly because the doping increases the electron density at the W-atom, promoting electron transport.

The hydrogen adsorption energy (*H) serves as a significant descriptor for evaluating the efficiency of various catalysts in the HER process.[46,47] The active site of the catalyst was investigated through a charge density difference (CDD) plot, where the O-site of $Cu(OH)_2$ acts as an active site with the charge accumulation region (Fig. S17†). From the CDD, it was also observed that the electron density at the O-atom of the Se-doped system is lower than that of the pristine one. The hydrogen atom is bonded with the O-atom with calculated free energy −0.21 and −0.17 eV for CuO/WO_3/$Cu(OH)_2$ and CuO/Se@WO_3/$Cu(OH)_2$, respectively, as shown in Fig. 4(d). Our results indicate that CuO/Se@WO_3/$Cu(OH)_2$ showed improved HER efficiency as $|G_H| < 0.20$ eV.[30] The calculated H adsorption-free energy of Pt(111) was reported to be −0.09 eV,[48] −0.15 eV,[49] or −0.17 eV,[50] which subsequently followed the Volmer–Tafel mechanism.[47] Since the calculated free energy for CuO/Se@WO_3/$Cu(OH)_2$ in our system is −0.17 eV, it is predicted to follow the Volmer–Tafel mechanism.

To evaluate the electrocatalytic activities of the oxygen evolution reaction (OER), we have calculated the free energy changes of the intermediates such as ΔG_{*OH} (ΔG_1), ΔG_{*O} (ΔG_2), and ΔG_{*OOH}(ΔG_3). Ideal OER electrocatalysts are defined by energy barriers of 1.23 eV for two adjacent elementary steps and an η-OER value of zero.[42] For instance, ΔG_1, ΔG_2, and ΔG_3 of CuO/WO_3/$Cu(OH)_2$ in the OER are 3.27, 1.32, and 2.0 respectively, while it is 3.25, 1.29, and 2.11 eV for CuO/Se@WO_3/$Cu(OH)_2$ as displayed in Fig. 4(e and f). Thus, the first step (H_2O–OH*) is the most energy-consuming, and it is the potential determining step (PDS) with the overpotential (η) 2.04 and 2.02 eV for CuO/WO_3/$Cu(OH)_2$ and CuO/Se@WO_3/$Cu(OH)_2$, respectively. The results clearly showed that Se-doping had minimal effect on the OER activity of the catalyst; however, the overpotential (η) of the systems in this work is found to be lower than many previously reported electrocatalysts.[51,52] Fig. S18 and S19† show all the stable adsorption configurations with stable adsorption distances obtained from potential energy curves (PECs). For better understanding, we have provided a detailed

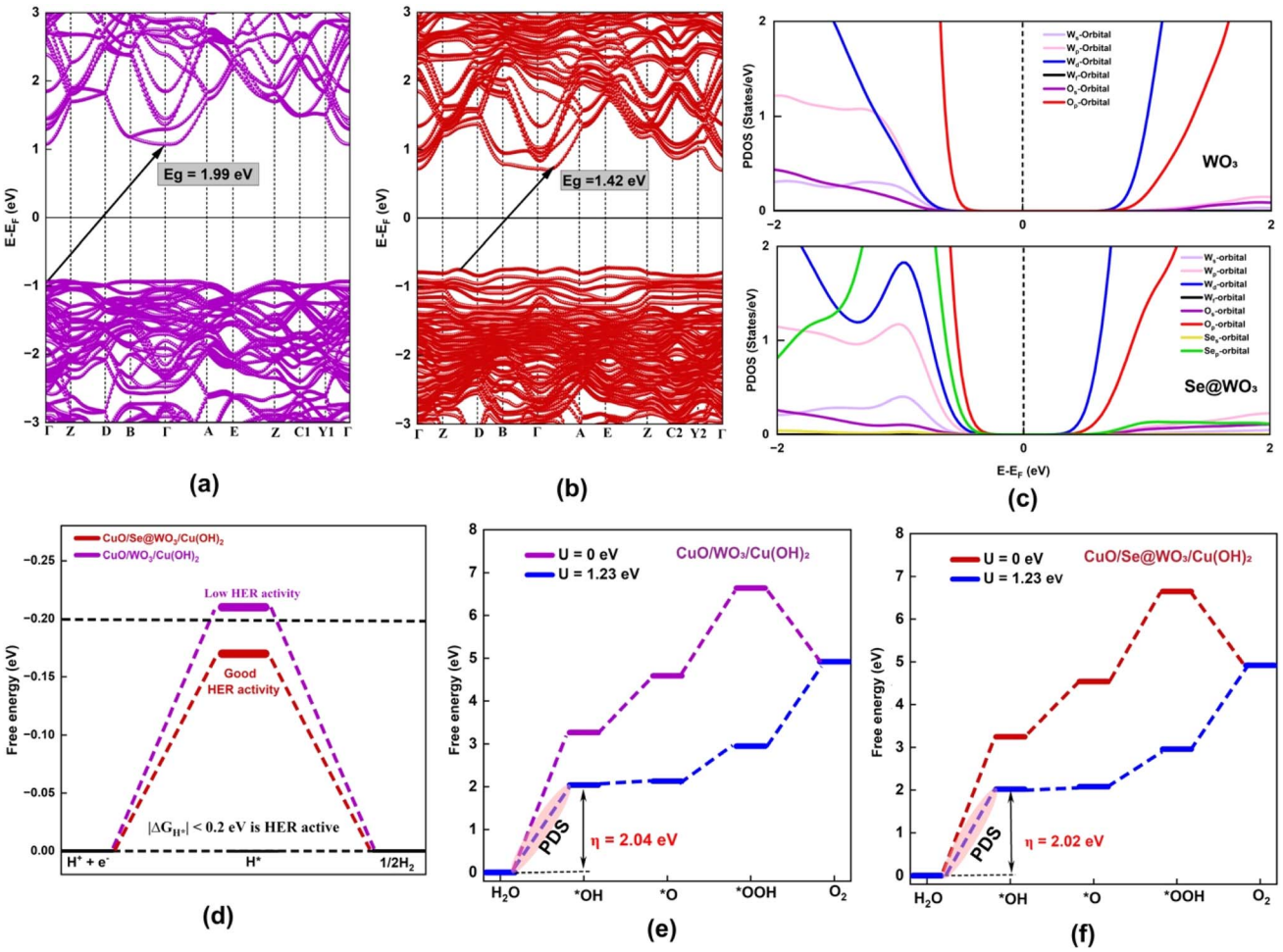

Fig. 4 Electronic band structures of (a) WO_3, (b) Se@WO_3, and (c) projected density of states (PDOS) plots of WO_3 and Se@WO_3. Free energy profile for the (d) HER and (e and f) OER in CuO/WO_3/Cu(OH)$_2$ and CuO/Se@WO_3/Cu(OH)$_2$.

in-depth discussion in Section 15 of the ESI,† comparing the calculated HER/OER performance (from DFT) with the experimentally measured performance.

4. Conclusions

In summary, the CuO/Se@WO_3/Cu(OH)$_2$ catalyst system on Ni foam demonstrates a significant advancement in electrocatalytic water splitting through strategic structural and electronic modifications. The dendritic CuO base layer, combined with Se-doped WO_3, forms a stable p–n junction that enhances electron mobility and reduces recombination, facilitated by a Z-scheme-like charge transfer mechanism. Selenium doping in WO_3 narrows the band gap by 0.54 eV, effectively increasing electron density at W_d orbitals and aligning the conduction band with CuO's valence band for efficient HER and OER. The addition of a Cu(OH)$_2$ layer further reduces charge transfer resistance by acting as a hole extractor, as evidenced by Tafel slopes of 35 mV dec^{-1} (OER) and 45 mV dec^{-1} (HER) and achieving overpotentials of 202 mV and 55 mV for the OER and HER, respectively, at 10 mA cm^{-2}. DFT calculations reinforce the experimental observations, showing that Se doping improves electronic conductivity and reduces the HER overpotential with $\Delta G_{H^*} = -0.17$ eV, enhancing the catalyst's performance compared to conventional RuO_2 for the OER and nearly matching Pt/C for the HER. The catalyst's robust performance under intermittent renewable energy conditions, attributed to its structural and electronic stability, highlights its promise as a scalable, cost-effective solution for sustainable hydrogen production in water electrolysis systems. This study underscores the value of band gap tuning and interfacial engineering in electrocatalysis, paving the way for next-generation bifunctional catalysts.

Data availability

The data supporting this article have been included as part of the ESI.†

Author contributions

Nitul Kalita conceptualized the study and led the experimental design. Theoretical studies were carried out by Upasana Nath and Manabendra Sarma, while Anjana Singha performed the DRT analysis. Mohammad Qureshi contributed to overall

coordination including funding and critical review of the manuscript including data analysis. All the authors have approved the final draft of the manuscript.

Conflicts of interest

The authors declare no competing financial interests.

Acknowledgements

Research support was provided to MQ by the Department of Science and Technology (SERB), India through the grant code SERB/CRG/2020/00211. NK gratefully acknowledges the Prime Minister's Research Fellowship (PMRF). All authors acknowledge the Supercomputing facility 'PARAM-Ishan' and National Supercomputing Mission (NSM) for providing computing resources of 'PARAM Kamrupa' at IIT Guwahati, which is implemented by C-DAC and supported by the Ministry of Electronics and Information Technology (MeitY) and the Department of Science and Technology (DST), Government of India. UN acknowledges the support from the Department of Science and Technology (DST), India, for an INSPIRE Fellowship (No. DST/INSPIRE Fellowship/2018/IF180745). We would like to acknowledge the central instrument facility at IIT Guwahati for providing us the instruments for successful characterization of the samples.

References

1 B. You and Y. Sun, Innovative Strategies for Electrocatalytic Water Splitting, *Acc. Chem. Res.*, 2018, **51**, 1571.
2 B. Suryanto, R. H, Y. Wang, R. K. Hocking, W. Adamson and C. Zhao, Overall Electrochemical Splitting of Water at the Heterogeneous Interface of Nickel and Iron Oxide, *Nat. Commun.*, 2019, **10**, 5599.
3 C. Lv, X. Wang, L. Gao, A. Wang, S. Wang, R. Wang, X. Ning, Y. Li, D. W. Boukhvalov, Z. Huang and C. Zhang, Triple Functions of $Ni(OH)_2$ on the Surface of WN Nanowires Remarkably Promoting Electrocatalytic Activity in Full Water Splitting, *ACS Catal.*, 2020, **10**, 13323.
4 A. Kundu, S. Gautam and B. Chakraborty, Mode of Electroactive Species Evolution from Fe_3X_4 (X = Se, S, O): Guidelines from the Redox Chemistry of Chalcogen Anions, *J. Mater. Chem. A*, 2024, **13**, 2920.
5 J. Jiao, W. Yang, Y. Pan, C. Zhang, S. Liu, C. Chen and D. Wang, Interface Engineering of Partially Phosphidated Co@Co–P@NPCNTs for Highly Enhanced Electrochemical Overall Water Splitting, *Small*, 2020, **16**, 2002124.
6 T. Tang, W. J. Jiang, S. Niu, N. Liu, H. Luo, Q. Zhang, W. Wen, Y. Y. Chen, L. B. Huang, F. Gao and J. S. Hu, Kinetically Controlled Coprecipitation for General Fast Synthesis of Sandwiched Metal Hydroxide Nanosheets/Graphene Composites toward Efficient Water Splitting, *Adv. Funct. Mater.*, 2018, **28**, 1704594.
7 F. Wang, L. Xiao, Y. Jiang, X. Liu, X. Zhao, Q. Kong, A. Abdukayum and G. Hu, Recent Achievements in Noble Metal-Based Oxide Electrocatalysts for Water Splitting, *Mater. Horiz.*, 2025, DOI: 10.1039/D4MH01315H.
8 P. Zhai, Y. Zhang, Y. Wu, J. Gao, B. Zhang, S. Cao, Y. Zhang, Z. Li, L. Sun and J. Hou, Engineering Active Sites on Hierarchical Transition Bimetal Oxides/Sulfides Heterostructure Array Enabling Robust Overall Water Splitting, *Nat. Commun.*, 2020, **11**, 5462.
9 K. Fan, H. Zou, Y. Lu, H. Chen, F. Li, J. Liu, L. Sun, L. Tong, M. F. Toney, M. Sui and J. Yu, Direct Observation of Structural Evolution of Metal Chalcogenide in Electrocatalytic Water Oxidation, *ACS Nano*, 2018, **12**, 12369.
10 R. Q. Li, S. Guo, X. Wang, X. Wan, S. Xie, Y. Liu, C. Wang, G. Zhang, J. Cao, J. Dai, M. Ge and W. Zhang, Dual-Strategy Engineered Nickel Phosphide for Achieving Efficient Hydrazine-Assisted Hydrogen Production in Seawater, *Chem. Sci.*, 2024, **15**, 10084.
11 S. Anantharaj, S. R. Ede, K. Sakthikumar, K. Karthick, S. Mishra and S. Kundu, Recent Trends and Perspectives in Electrochemical Water Splitting with an Emphasis on Sulfide, Selenide, and Phosphide Catalysts of Fe, Co, and Ni: A Review, *ACS Catal.*, 2016, **6**, 8069.
12 V. Vij, S. Sultan, A. M. Harzandi, A. Meena, J. N. Tiwari, W. G. Lee, T. Yoon and K. S. Kim, Nickel-Based Electrocatalysts for Energy-Related Applications: Oxygen Reduction, Oxygen Evolution, and Hydrogen Evolution Reactions, *ACS Catal.*, 2017, **7**, 7196.
13 B. Yan, D. Krishnamurthy, C. H. Hendon, S. Deshpande, Y. Surendranath and V. Viswanathan, Surface Restructuring of Nickel Sulfide Generates Optimally Coordinated Active Sites for Oxygen Reduction Catalysis, *Joule*, 2017, **1**, 600.
14 Y. Zeng, Z. Cao, J. Liao, H. Liang, B. Wei, X. Xu, H. Xu, J. Zheng, W. Zhu, L. Cavallo and Z. Wang, Construction of Hydroxide p–n Junction for Water Splitting Electrocatalysis, *Appl. Catal., B*, 2021, **292**, 120160.
15 S. Bhowmick, A. Sarangi, C. T. Moi, S. Chakraborty and M. Qureshi, Diffusion-Mediated Morphological Transformation in Bifunctional Mn_2O_3/CuO-$(VO)_3(PO_4)_2 \cdot 6H_2O$ for Enhanced Electrochemical Water Splitting, *ACS Appl. Mater. Interfaces*, 2022, **14**, 52204.
16 S. M. Wu, L. Wu, N. Denisov, Z. Badura, G. Zoppellaro, X. Y. Yang and P. Schmuki, Pt Single Atoms on TiO_2 Can Catalyze Water Oxidation in Photoelectrochemical Experiments, *J. Am. Chem. Soc.*, 2024, **146**, 16363.
17 Z. Y. Liu, S. Jia, Y. Hu, Y. Fang, Y. Feng, D. Li, S. Bai, R. Luo and A. Chen, Facile One-Step Synthesis of a $WO_3/ZnWO_4$ Heterojunction Modified Using ZnFe LDH Enhances the PEC Water Splitting Efficiency, *Dalton Trans.*, 2024, **53**, 17059.
18 I. P. Seetoh, A. K. Ramesh, W. X. Tan and C. Q. Lai, Enhanced Photoelectrochemical Water Splitting Using Carbon Cloth Functionalized with ZnO Nanostructures via Polydopamine Assisted Electroless Deposition, *Nanoscale*, 2024, **16**, 8401.
19 M. Dhillon, A. Naskar, N. Kaushal, S. Bhansali, A. Saha and A. K. Basu, A Novel GO Hoisted SnO_2-BiOBr Bifunctional Catalyst for the Remediation of Organic Dyes under

Illumination by Visible Light and Electrocatalytic Water Splitting, *Nanoscale*, 2024, **16**, 12445.

20 D. Ghosh, D. K. Bora and A. B. Panda, Enhanced Electrocatalytic Overall Alkaline Water Splitting Induced by Interfacial Electron Coupling of Mn_3O_4 Nano-Cube@CeO_2/γ-FeOOH Nanosheet Hetero-Structure, *J. Mater. Chem. A*, 2024, **12**, 30783.

21 S. Zhao, C. Jia, X. Shen, R. Li, L. Oldham, B. Moss, B. Tam, S. D. Pike, N. Harrison, E. A. Ahmad and A. Kafizas, The Aerosol-Assisted Chemical Vapour Deposition of Mo-Doped $BiVO_4$ Photoanodes for Solar Water Splitting: An Experimental and Computational Study, *J. Mater. Chem. A*, 2024, **12**, 26645.

22 M. Yang, Z. Fan, J. Du, C. Feng, R. Li, B. Zhang, N. Pastukhova, M. Valant, M. Finšgar, A. Mavrič and Y. Li, Designing Atomic Interface in Sb_2S_3/CdS Heterojunction for Efficient Solar Water Splitting, *Small*, 2024, **20**, 2311644.

23 L. A. Ramos-Huerta, O. Aguilar-Martínez, V. Santes, F. J. Tzompantzi Morales and C. E. Santolalla-Vargas, Time-Dependent Synthesis of ZnS and Its Influence on Photocatalytic Hydrogen Generation, *Chem. Eng. Sci.*, 2024, **294**, 120067.

24 M. Kumar and T. C. Nagaiah, A NiCu-MoS_2 Electrocatalyst for PH-Universal Hydrogen Evolution Reaction and Zn-Air Batteries Driven Self-Power Water Splitting, *J. Mater. Chem. A*, 2023, **11**, 18336.

25 C. Guo, H. Xue, J. Sun, N. Guo, T. Song, J. Sun, Y. R. Hao and Q. Wang, A Co_2N/CoP p–n Junction with Modulated Interfacial Charge and Rich Nitrogen Vacancy for High-Efficiency Water Splitting, *Chem. Eng. J.*, 2023, **470**, 144242.

26 S. Adhikari, S. N. Steinmann, M. Arunachalam, S. H. Kang and D. H. Kim, Unraveling the Oxidation Kinetics Through Electronic Structure Regulation of $MnCo_2O_{4.5}$@Ni_3S_2 p–n Junction for Urea-Assisted Electrocatalytic Activity, *Small*, 2024, **20**, 2311548.

27 Y. C. Wang, C. Y. Chang, T. F. Yeh, Y. L. Lee and H. Teng, Formation of Internal P-n Junctions in Ta_3N_5 Photoanodes for Water Splitting, *J. Mater. Chem. A*, 2014, **2**, 20570.

28 Z. Feng, F. Lu, Q. Hu, J. Qiu, X. Lei, B. Wang, R. Guo, Y. Tian, X. Liu and J. You, Built-in Electric Fields and Extra Electric Fields in the Oxygen Evolution Reaction, *J. Mater. Chem. A*, 2024, **12**, 18047.

29 N. Kalita, A. Sahu, S. Bhowmick and M. Qureshi, Synchronized Redox Pairs in Metal Oxide/Hydroxide Chemical Analogues for an Efficient Oxygen Evolution Reaction, *Chem. Commun.*, 2022, **58**, 13747.

30 J. Zhang, D. Li, L. Ju, G. Yang, D. Yuan, Z. Feng and W. Wang, The Charge Effects on the Hydrogen Evolution Reaction Activity of the Defected Monolayer MoS_2, *Phys. Chem. Chem. Phys.*, 2023, **25**, 10956.

31 S. Niu, S. Li, Y. Du, X. Han and P. Xu, How to Reliably Report the Overpotential of an Electrocatalyst, *ACS Energy Lett.*, 2020, **5**, 1083.

32 G. Kresse and J. Furthmiiller, Efficiency of Ab-Initio Total Energy Calculations for Metals and Semiconductors Using a Plane-Wave Basis Set, *Comput. Mater. Sci.*, 1996, **6**, 15.

33 G. Kresse and J. Furthmü, Efficient Iterative Schemes for Ab Initio Total-Energy Calculations Using a Plane-Wave Basis Set, *Phys. Rev. B:Condens. Matter Mater. Phys.*, 1996, **54**, 17953.

34 J. P. Perdew, K. Burke and M. Ernzerhof, Generalized Gradient Approximation Made Simple, *Phys. Rev. Lett.*, 1996, **77**, 3865.

35 P. E. Blochl, Projector Augmented-+rave Method, *Phys. Rev. Lett.*, 1994, **50**, 17953.

36 H. J. Monkhorst and J. D. Pack, Special Points for Brillonin-Zone Integrations, *Phys. Rev. B*, 1976, **13**, 5188.

37 S. Grimme, J. Antony, S. Ehrlich and H. Krieg, A Consistent and Accurate Ab Initio Parametrization of Density Functional Dispersion Correction (DFT-D) for the 94 Elements H-Pu, *J. Chem. Phys.*, 2010, **132**, 154104.

38 X. Zhou, H. Dong and A. M. Ren, The Mechanism of Hydrogen and Oxygen Evolution Reaction in Ni-NiO/β-Ga_2O_3 Photocatalyst, *Int. J. Hydrogen Energy*, 2016, **41**, 5670.

39 J. K. Nørskov, J. Rossmeisl, A. Logadottir, L. Lindqvist, J. R. Kitchin, T. Bligaard and H. Jónsson, Origin of the Overpotential for Oxygen Reduction at a Fuel-Cell Cathode, *J. Phys. Chem. B*, 2004, **108**, 17886.

40 L. Cao, Q. Luo, W. Liu, Y. Lin, X. Liu, Y. Cao, W. Zhang, Y. Wu, J. Yang, T. Yao and S. Wei, Identification of Single-Atom Active Sites in Carbon-Based Cobalt Catalysts during Electrocatalytic Hydrogen Evolution, *Nat. Catal.*, 2019, **2**, 134.

41 N. H. Kwon, M. Kim, X. Jin, J. Lim, I. Y. Kim, N. S. Lee, H. Kim and S. J. Hwang, A Rational Method to Kinetically Control the Rate-Determining Step to Explore Efficient Electrocatalysts for the Oxygen Evolution Reaction, *NPG Asia Mater.*, 2018, **10**, 659.

42 G. Li, J. Yu, W. Yu, L. Yang, X. Zhang, X. Liu, H. Liu and W. Zhou, Phosphorus-Doped Iron Nitride Nanoparticles Encapsulated by Nitrogen-Doped Carbon Nanosheets on Iron Foam In Situ Derived from Saccharomycetes Cerevisiae for Electrocatalytic Overall Water Splitting, *Small*, 2020, **16**, 2001980.

43 Y. Lu, C. Z. Zhao, J. Q. Huang and Q. Zhang, The Timescale Identification Decoupling Complicated Kinetic Processes in Lithium Batteries, *Joule*, 2022, **6**, 1172.

44 C. Sheng, F. Yu, C. Li, H. Zhang, J. Huang, Y. Wu, M. Armand and Y. Chen, Diagnosing the SEI Layer in a Potassium Ion Battery Using Distribution of Relaxation Time, *J. Phys. Chem. Lett.*, 2021, **12**, 2064.

45 Y. Ma, B. Feng, J. Lang, F. Wang and Y. H. Hu, Synthesis of Semimetallic Tungsten Trioxide for Infrared Light Photoelectrocatalytic Water Splitting, *J. Phys. Chem. C*, 2019, **123**, 25833.

46 P. Ramirez-Vidal, R. L. S. Canevesi, G. Sdanghi, S. Schaefer, G. Maranzana, A. Celzard and V. Fierro, A Step Forward in Understanding the Hydrogen Adsorption and Compression on Activated Carbons, *ACS Appl. Mater. Interfaces*, 2021, **13**, 12562.

47 E. Skúlason, V. Tripkovic, M. E. Björketun, S. Gudmundsdóttir, G. Karlberg, J. Rossmeisl, T. Bligaard, H. Jónsson and J. K. Nørskov, Modeling the

Electrochemical Hydrogen Oxidation and Evolution Reactions on the Basis of Density Functional Theory Calculations, *J. Phys. Chem. C*, 2010, **114**, 18182.

48 Y. Zheng, Y. Jiao, Y. Zhu, L. H. Li, Y. Han, Y. Chen, A. Du, M. Jaroniec and S. Z. Qiao, Hydrogen Evolution by a Metal-Free Electrocatalyst, *Nat. Commun.*, 2014, **5**, 3783.

49 N. Dubouis and A. Grimaud, The Hydrogen Evolution Reaction: From Material to Interfacial Descriptors, *Chem. Sci.*, 2019, **10**, 9165.

50 C. Tsounis, B. Subhash, P. V. Kumar, N. M. Bedford, Y. Zhao, J. Shenoy, Z. Ma, D. Zhang, C. Y. Toe, S. Cheong, R. D. Tilley, X. Lu, L. Dai, Z. Han and R. Amal, Pt Single Atom Electrocatalysts at Graphene Edges for Efficient Alkaline Hydrogen Evolution, *Adv. Funct. Mater.*, 2022, **32**, 2203067.

51 A. Ostadhossein, J. Guo, F. Simeski and M. Ihme, Functionalization of 2D Materials for Enhancing OER/ORR Catalytic Activity in Li–Oxygen Batteries, *Commun. Chem.*, 2019, **2**, 95.

52 N. Yao, H. Jia, J. Zhu, Z. Shi, H. Cong, J. Ge and W. Luo, Atomically Dispersed Ru Oxide Catalyst with Lattice Oxygen Participation for Efficient Acidic Water Oxidation, *Chem*, 2023, **9**, 1882.